

**Eccentric black hole-neutron star mergers: Effects of black hole spin and equation of state**William E. East,<sup>1</sup> Frans Pretorius,<sup>1</sup> and Branson C. Stephens<sup>2</sup><sup>1</sup>*Department of Physics, Princeton University, Princeton, New Jersey 08544, USA*<sup>2</sup>*Center for Gravitation and Cosmology, University of Wisconsin-Milwaukee, Milwaukee, Wisconsin 53211, USA*

(Received 14 November 2011; published 5 June 2012)

There is a high level of interest in black hole-neutron star binaries, not only because their mergers may be detected by gravitational wave observatories in the coming years, but also because of the possibility that they could explain a class of short duration gamma-ray bursts. We study black hole-neutron star mergers that occur with high eccentricity as may arise from dynamical capture in dense stellar regions such as nuclear or globular clusters. We perform general relativistic simulations of binaries with a range of impact parameters, three different initial black hole spins (zero, aligned and antialigned with the orbital angular momentum), and neutron stars with three different equations of state. We find a rich diversity across these parameters in the resulting gravitational wave signals and matter dynamics, which should also be reflected in the consequent electromagnetic emission. Before tidal disruption, the gravitational wave emission is significantly larger than perturbative predictions suggest for periastris distances close to effective innermost stable separations, exhibiting features reflecting the zoom-whirl dynamics of the orbit there. Guided by the simulations, we develop a simple model for the change in orbital parameters of the binary during close-encounters. Depending upon the initial parameters of the system, we find that mass transfer during nonmerging close-encounters can range from essentially zero to a sizable fraction of the initial neutron star mass. The same holds for the amount of material outside the black hole post-merger, and in some cases roughly half of this material is estimated to be unbound. We also see that nonmerging close-encounters generically excite large oscillations in the neutron star that are qualitatively consistent with  $f$ -modes.

DOI: [10.1103/PhysRevD.85.124009](https://doi.org/10.1103/PhysRevD.85.124009)

PACS numbers: 04.25.D-

**I. INTRODUCTION**

It is important to understand mergers of black holes (BHs) and neutron stars (NSs) not only because they are a chief source for ground-based gravitational wave (GW) detectors (such as LIGO [1]), but also because they may be accompanied by a diverse range of electromagnetic (EM) and neutrino emission. One of the more interesting possibilities in this regard is that BH-NS mergers may be progenitors of a fraction of observed short-hard gamma-ray bursts (sGRBs) [2–4]. Furthermore, existing and planned wide-field survey telescopes such as PTF [5], Pan-STARRS [6], and LSST [7] are beginning to observe and classify fainter EM transient events, some of which are expected to be produced in BH-NS mergers from a variety of mechanisms (see [8] for a recent, detailed exploration of the possibilities). Coincident observation of these EM events with a gravitational wave signal from a binary coalescence would provide a wealth of additional information about the system beyond any individual observation, even, for example, providing an independent way to measure cosmological parameters [9]. However this depends on having a good understanding of how to map the particular observations to the underlying astrophysical processes governing the merger.

The great diversity in sGRBs hints at the possibility that there will be a corresponding diversity in the associated GW and EM signals, and motivates the exploration of all

viable channels for binary compact (BCO) mergers. BCOs may form through the evolution of primordial binaries or through dynamical capture in dense stellar systems, such as nuclear or globular clusters. BCOs formed through the latter channel, which could merge with non-negligible eccentricity are the focus of this work, which is a follow-up of a first study of dynamical capture BH-NS evolution using full general relativistic hydrodynamics [10]. Before delving into the details, we briefly summarize the motivation for studying this class of BCO; see [10] and a related study on eccentric NS-NS mergers [11] for more discussion. In contrast, most studies of BH-NS mergers to date have focused on the quasicircular inspiral case; see [12] for a review of these efforts.

A chance close-encounter of a BH and NS in a stellar cluster could result in a bound system if the energy loss due to GW emission is sufficiently large. (Tidal interaction with the NS is also a source of energy loss [13], though due to the relative scalings with distance, to leading-order the total cross section for *capture* is dominated by the GW emission.) Because of gravitational focusing, a sizable fraction of binding encounters will result in highly eccentric binaries that merge within a few orbits of the initial encounter. For Newtonian hyperbolic orbits of systems with total mass  $M$  and relative velocity  $w$  at infinity, the pericenter separation  $r_p$  is related to the impact parameter at infinity  $b$  by  $r_p = b^2 w^2 / 2M + O(w^4)$  (unless otherwise stated we employ geometric units with  $G = c = 1$

throughout). Thus, since the capture rate is linearly proportional to the cross sectional area, it is linearly proportional to  $r_p$ . For the 4:1 BH to NS mass ratio systems studied here (with  $w = 1000$  km/s), estimates of the energy lost to GW based on the work of [14] shows binding encounters occur at  $r_p \lesssim 40M$  (and scales with mass ratio as  $\mu^{4/7}$ ). The results presented here show that cases with initial  $r_p \lesssim 7M$  (for the canonical nonspinning BH), or close to 20% of binding encounters (of a 4:1 system with  $w = 1000$  km/s), result in “direct collisions,” i.e. merging on the first close-encounter.

At first glance it may seem that such encounters would be too rare to be of any relevance as possible GW or EM transient sources; however, recent studies have suggested otherwise. In [15] estimates of BH-BH encounters in galactic nuclear clusters suggest Advanced LIGO rates of  $O(1-10^3)$  per year, while in [16] (following earlier work in [17–19]) it was argued that direct capture NS-NS mergers in globular clusters could account for a sizable fraction of observed sGRBs. In this latter work, a procedure is also provided for scaling the NS-NS results to BH-NS systems, which yields BH-NS dynamical capture event rates of  $O(10-10^2)$   $\text{yr}^{-1} \text{Gpc}^{-3}$  (using an estimate of the relative fraction of BH to NSs  $f_{\text{BH}}/f_{\text{NS}} \approx 0.28$  as suggested in [16]). In comparison, population synthesis models [20] find primordial BH-NS merger rates from  $\sim 0.1 \text{ yr}^{-1} \text{Gpc}^{-3}$  (pessimistic) to  $\sim 120 \text{ yr}^{-1} \text{Gpc}^{-3}$  (optimistic). To estimate Advanced LIGO detection rates would require full templates for these events, which we relegate to a future study; however, in [21] the signal-to-noise ratio was computed using post-Newtonian-based models of the early stages of the mergers, which showed that a subset (depending upon the component masses) could be observed out to 200–300 Mpc for an average orientation, even excluding the final stages of the merger in the templates. This suggests detection rates of  $\sim 0.3-10/\text{yr}$ . For comparison to primordial BH/NS binaries, [22] quotes an Advanced LIGO optimal detection distance of 927 Mpc for a  $10M_{\odot}$  BH to  $1.4M_{\odot}$  NS merger, which scales to  $\sim 400$  Mpc when averaging over orientation and sky location; the corresponding detection rates range from 0.2/yr to 300/yr for pessimistic to optimistic source population estimates.

Though far from conclusive, there is also observational evidence for multiple sGRB progenitors, which could, in part, be due to dynamical capture vs primordial mergers. Of sGRBs with identified host galaxies,  $\sim 25\%$  have offsets of  $\geq 15$  kpc from their hosts [23]. This subset of sGRBs with large offsets would be consistent with kicked, primordially formed BCOs or with dynamically formed binaries in globular clusters. The latter may be preferred for the largest offsets [24], especially if primordial BCOs experience weak kicks [25]. Analysis of x-ray afterglows observed by Swift/X-Ray Telescope suggests that different progenitors may be responsible for sGRBs with and without extended emission [26]; again, one possible

explanation is dynamical capture (with extended tidal tails leading to long-term emission) vs primordial. There has also been a claim that a very high-energy gamma-ray source observed in Terzan 5 may, in fact, be the remnant of a BCO merger-powered sGRB [27]; if true, this would support the claim that dense cluster environments can be significant sources of BCO mergers.

It has also been suggested that some merging NS-NS or BH-NS binaries are actually part of a coeval or dynamically formed triple [28]. The tertiary (for example a white dwarf) drives the binary to high eccentricities through a Kozai resonance, resulting in a faster merger time. Though dynamically different from direct capture two-body systems, in Kozai-accelerated evolution the merger itself could take place with significant eccentricity [29] and have comparable behavior at late times to the systems studied here. However, we are unaware of any systematic studies of expected populations and corresponding LIGO-event rates for such Kozai triple systems.

Merging with moderate to high eccentricity could have significant effects on all the GW and EM observables from the event. In contrast to a low-eccentricity inspiral, the GWs are emitted primarily around periastron, resulting in waveforms that resemble a sequence of bursts more than a continuous signal. Consequently, for mass ratios relevant to stellar mass BH-NS mergers, the evolution of effective orbital parameters describing the binary is not adiabatic, i.e. it does not occur quasistatically as in the early inspiral of low-eccentricity binaries. Regarding effects associated with tidal disruption of the NS, an interesting coincidence for this class of BH-NS systems is that the typical radii inside of which tidal stripping begins, depending upon the NS compactness and, hence, equation of state (EOS), roughly coincides with the range of pericenter separations where the orbit becomes unstable due to general relativistic effects ( $r_p \lesssim 10M$  depending upon on the spin of the black hole where  $M$  is the total mass of the system). The resultant dynamics could thus be very different from Newtonian expectations. Of course, these two zones also roughly correspond for quasicircular inspiral. However, highly eccentric binaries have significantly more angular momentum (at a given orbital separation) than quasicircular binaries. This additional angular momentum could strongly affect the matter dynamics relative to the quasicircular case, for example, resulting in comparatively massive disks and/or in multiple and prolonged episodes of mass transfer and ejection. Ejected mass will decompress and form heavy elements through the  $r$ -process [30–32], and thus these systems could account for a significant fraction of such elements in the Universe. Furthermore, subsequent decay of the more radioactive isotopes could lead to observable EM counterparts [8,33].

In [10] we presented the first simulations of BH-NS hyperbolic capture and merger for a nonspinning BH and a single equation of state, modeled using general

relativistic hydrodynamics (GRHD) (see [16] for an earlier related study using a Newtonian-based hydrodynamics code). We found a striking dependence of the outcome—disk mass, unbound material, GW signal—on the impact parameter. However, astrophysical BHs are expected to form with a range of spins, (see e.g. [34,35]) and in the quasicircular case spin was found to be crucial in obtaining significant accretion disks [36–39]. Additionally, there is significant uncertainty about the NS equation of state. Since the EOS determines the NS compaction and, hence, the point at which the NS will become tidally disrupted, it is also an important determinant of the merger outcome. Here, we expand upon the previous analysis and consider initial BH-spins aligned and antialigned with the orbital angular momentum (with dimensionless spin parameter  $a = 0.5$  and  $a = -0.5$ , respectively), as well as different EOSs (the “2H”, “HB” and “B” models from [40]). Note that there is no *a priori* reason to expect alignment of the BH spin with orbital angular momentum in dynamical-capture binaries; this particular choice of spin direction and magnitude was purely motivated as a first, simple exploration of the effects of spin on the merger. Certainly in future studies a broader expanse of parameters will need to be considered. There is also much room for improvement with the matter description, including more realistic EOSs and additional physics beyond GRHD. For quasicircular BH-NS inspiral [41], EOS effects were studied in [42–45], the effects of magnetic fields in [46,47], and higher mass ratio systems (up to 7:1) in [48].

In the remainder of the paper we begin with a brief review of our numerical methods (Sec. II); more details are given in a companion paper [49]. In Sec. III, we describe the particular cases we study. We focus on systems with small initial periapsis  $r_p$ , in part for the practical reason that these binaries merge quickly and are thus computationally tractable, this is the regime where full general-relativistic effects will be most strongly manifested, and because maximum complementary information to post-Newtonian studies (e.g. [21] or [16]) can be obtained. We present the results of the simulations in Sec. IV. We find that the rich variability in the dynamics and merger outcome as a function of impact parameter is compounded by considering different EOSs and values of BH spin. For example, we find that with prograde spin or a stiffer EOS significant episodes of mass transfer may occur during nonmerger close-encounters. Systems where the BH has retrograde spin or that are somewhat less eccentric (than parabolic) can undergo sustained whirling phases before merger that are evident in the GW signal. As in the eccentric binary NS mergers studied in [11], we also find that strong  $f$ -mode oscillations in the NS can be excited in close, nonmerger encounters (see also an earlier study of a head-on BH-NS collision [50], though here the presence of the  $f$ -mode is largely a consequence of the initial data). In Sec. V we use the results of the simulations to calibrate a

simple model for the nonadiabatic evolution of effective orbital parameters during each close-encounter. This will be used in a future study to build model GW templates and explore the detectability of these systems with gravitational wave observations. We conclude in Sec. VI.

## II. NUMERICAL METHODS

In this section, we briefly outline our numerical methods for solving the GRHD equations. More details are presented in [49], including results from an extensive range of tests.

### A. Evolution

We model the evolution of BH-NS binaries by solving the Einstein field equations coupled to a perfect fluid. We solve the field equations in the generalized harmonic form [51–53] with constraint damping [54,55], where the coordinate degrees of freedom are specified through source functions  $H^a$ . We employ fourth-order accurate finite difference (FD) techniques and Runge-Kutta time-stepping. In order to avoid singularities, we excise within any apparent horizons. In evolving eccentric binaries, we find that a damped harmonic gauge similar to the one described in [56] (see also [57]) is beneficial for achieving stable evolutions through merger. Specifically, a damped harmonic gauge takes the form  $H^a = \xi(n^a - \bar{n}^a)$ , where  $n^a$  is the four-vector normal to the constant coordinate time slices,  $\bar{n}^a$  is another timelike unit vector, and  $\xi$  is a constant controlling the magnitude of the damping. The particular form for  $\bar{n}^a$  that we found to work well is from [57],

$$\bar{n}^a = \frac{1}{\alpha} \left( \frac{\partial}{\partial t} \right)^a + \log \left( \frac{\alpha}{h^{1/2}} \right) n^a. \quad (1)$$

We use a value of  $\xi \approx 0.2/M$ , though include a spatial dependency so that  $\xi$  goes to zero at spatial infinity. In addition, we begin with initial data in the harmonic gauge and transition to this damped harmonic gauge before the two objects begin to strongly interact. The use of this gauge seems to smooth out sharp features in the lapse that develop near merger when harmonic gauge is used, however, we have not studied the pure harmonic case in sufficient detail to conclude whether or not harmonic time slicing is developing a coordinate singularity.

We describe the neutron star material as a perfect fluid. The fluid equations are written in conservation-law form and solved using high-resolution shock-capturing schemes. Though we have implemented several methods for calculating intercell fluxes and for reconstructing fluid primitive variables at cell faces, we used HLL [58] combined with WENO-5 [59] for the results presented here. The fluid is evolved with outflow-boundary conditions using second-order Runge-Kutta time-stepping. To resolve the various length scales, we use Berger- and Oliger-style adaptive mesh refinement (AMR) [60]. AMR boundaries require special treatment in conservative hydrodynamics codes,

since the fluxes emerging from a fine-grid region, for example, do not exactly match the incoming flux calculated on the coarse grid due to their differing truncation errors. To enforce conservation, we correct the adjacent coarse-grid cells using the fine-grid fluxes, according to the method of Berger and Colella [61]; more details on our particular implementation of this method is given in [49].

Truncation error estimates are used to generate the AMR-level structure. All initial data were evolved with a fiducial “medium” resolution run, where the coarsest-level has  $128^3$  cells and covers the entire domain (we use a compactified coordinate system, so this includes spatial infinity). We also chose a maximum truncation error so that initially six additional levels of refinement (seven total) are generated to resolve the BH and NS. Given the computational expense of these simulations, we limited the total number of levels to seven during evolution, and did not allow regridding on the two coarsest-levels to prevent the algorithm from tracking the outgoing gravitational waves beyond the largest extraction sphere of  $100M$ . For several representative cases we also ran a “low” and “high” resolution simulation for convergence testing, where on each level the low (high) resolution run had a mesh spacing of  $64/50$  ( $64/96$ ) of the medium resolution run, and we scaled the corresponding maximum local-truncation error threshold-parameter used by the AMR algorithm assuming second-order convergence. Note that this procedure will not generate identical hierarchies between different resolution runs (except for the two coarsest levels in the wave zone, which we keep fixed), but on average the highest-resolution grid covering a given coordinate cell will have the above refinement ratios between the different runs. To give some sense of the smallest scales resolved by the hierarchy, before tidal disruption, the low (medium, high) resolution run has two finest-level meshes centered around the BH and NS of roughly  $80^3$  ( $100^3$ ,  $150^3$ ) cells each, resolving the diameter of the NS with approximately 40 (50, 75) cells and the BH horizon diameter with roughly 70 (85, 130) cells. Unless otherwise noted, results will be reported for medium resolution with error bars (where appropriate) computed from convergence calculations.

## B. Initial data

We construct initial data by superimposing a boosted BH with a boosted nonspinning Tolman-Oppenheimer-Volkoff star solution separated by  $d = 50M$ . Though this superposition does not strictly satisfy the constraint equations except in the limit of infinite separation, we have performed tests at various separations in order to verify that the superposition-induced constraint violation is comparable to truncation error at our resolution, in particular, following an initially slightly larger transient that propagates away (and is partly damped due to the use of constraint damping) on roughly the light-crossing time  $d$  of the

binary. In Fig. 1, we show the level of constraint violation ( $C_a \equiv H_a - \square x_a$ ) following the transient for various separations and resolutions for the  $r_p = 10M$  case. At these resolutions, we can still achieve convergence of the constraints with this superposed data, and increasing the initial separation to  $d = 100M$  does not significantly affect the level of constraint violation at the same resolution. This implies that the error introduced by the superposition is on the order of or smaller than the numerical truncation error at this resolution.

The fact that we are beginning the binary at finite separation as a simple superposition of boosted single-compact object solutions and that there is a transient early time constraint-violation, both effectively introduce systematic errors in the parameters of the binary. To give some idea of the possible magnitude of this error, the effect on the apparent horizon-mass of the BH at early times and the amplitude of the density oscillation induced in the NS are both  $\lesssim 2\%$ . Though it is difficult to exactly quantify how this will translate to modified-binary parameters, we expect it to be comparable to or smaller than the error introduced by setting initial orbital parameters at a finite distance based on a Newtonian approximation (as described in the next section). As we report later, the truncation error in quantities of interest that we do measure such as energy emitted in GWs is percentwise larger than this, implying that solving the constraints or attempting more

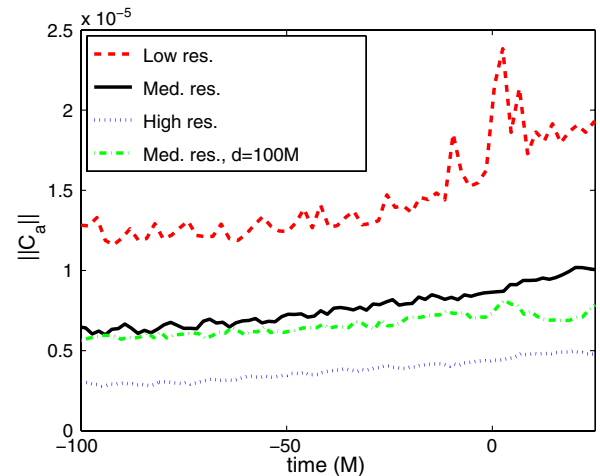


FIG. 1 (color online).  $L^2$ -norm of the constraint violation,  $C_a \equiv H_a - \square x_a$ , in units of  $1/M$  from the  $r_p = 10M$  case in the  $100M \times 100M$ -region around the center of mass in the equatorial plane (i.e.  $\sqrt{\int \|C_a\|^2 d^2x} / \int d^2x$ ). This is shown for low, medium, and high resolutions for the standard initial separation between the BH and NS of  $d = 50M$ ; the relative magnitudes at a given time are consistent to good approximation with second-order convergence. Also shown is a medium resolution run with an initial separation of  $d = 100M$ . The time is shifted so that the point of closest approach occurs at approximately  $t = 0$  for all cases.

accurate initial representations for the metric and NS fluid distribution may only offer marginal improvement in the overall accuracy of the results at these resolutions. However, for future higher-resolution studies it would be important to solve the constraints and improve the model of the physical initial conditions for the system.

Finally, we briefly comment that since our simulations employ compactified coordinates such that the outer boundaries extend to spatial infinity, the global (Arnowitt-Deser-Misner)  $M$ , and  $J$  should be conserved. In practice, however, we must evaluate these quantities at a finite distance, making them subject to gauge artifacts, some propagating outward from the central BH-NS region from  $t = 0$ . For  $t < 200M$ , an extraction sphere of  $300M$  is free of propagating artifacts, hence  $M$  ( $J$ ) is conserved to better than 0.3 (2.0)% for all cases at medium resolution.

### III. CASES

Motivated by possible BH-NS interactions in cores of galactic nuclei and globular clusters, we create initial data for hyperbolic encounters with varying impact parameter. These encounters are hyperbolic since the two bodies have nonzero kinetic energy at (effectively) infinite separation. We will take their relative velocity at infinity to be  $w = 1000$  km/s since this is the expected magnitude of the virial velocity in the core of a nuclear cluster [15,62].

In practice, this initially positive total energy is small compared to the kinetic energy of the encounter itself so that the orbits are nearly parabolic and have eccentricities  $1 + O(10^{-5})$ . In this study we also restrict our attention to BH-NS systems with a 4:1-mass ratio (referring to the isolated ADM masses of the BH and NS). The reasons for choosing this mass ratio are in part because it is within the range of astrophysically plausible values given current observations of NS and candidate BH masses (see, for example, [63,64]), and in part because within this range it is also a value where we expect to see strong tidal-disruption effects. Certainly it would be of interest to explore a broader range of mass ratios, however, due to limited computational resources we leave that to a future study.

We choose the initial positions and velocities for the BH and the NS according to the Newtonian equations for a hyperbolic orbit (see, e.g., [65]) with  $w = 1000$  km/s and an initial separation of  $d = 50M$ . We vary the initial spin of the BH, considering the values  $a = -0.5, 0$ , and  $0.5$  where negative (positive) values indicate retrograde (prograde) spin in relation to the orbital angular momentum. We also consider three  $\Gamma$ -law model EOSs labeled 2H, HB, and B in [40]. For the prototypical  $1.35M_{\odot}$  NS that we use, these EOSs give compactions of  $M_{\text{NS}}/R_{\text{NS}} = 0.13, 0.17$ , and  $0.18$ , respectively. Note that while the compaction of the B EOS NS is only slightly smaller than that of the HB, it has a maximum mass of  $2.0M_{\odot}$  (the 2H and HB have

maximum masses of  $2.83$  and  $2.12M_{\odot}$ , respectively). Given recent observations [66], B is therefore on the soft end of the allowed range for the EOS family considered here. We include a thermal component in the EOS, a  $\Gamma$ -law with  $\Gamma_{\text{th}} = 1.5$  to allow for shock heating.

We do not consider large impact parameters corresponding to initial  $r_p > 15M$ . Even so, for impact parameters at the upper end of the range that we do evolve, the eccentricity is sufficiently large (though  $< 1$ ) after the first close-encounter that it would be very expensive to evolve to the second encounter. To help calibrate our model for orbital parameter evolution that will be introduced in Sec. V, we also consider a set of runs with initial orbital parameters for a bound orbit with eccentricity  $e = 0.75$  instead of the hyperbolic orbit with  $e \approx 1$ . These simulations can be seen as corresponding to systems that have already undergone one or more close-encounters and evolved to these orbital parameters.

To keep the parameter space at a manageable size, we vary only one of the three parameters of BH spin, NS-EOS, and initial eccentricity at a time from our base case—an initially nonspinning BH ( $a = 0$ ), a NS with the HB EOS, and the two objects initially with Newtonian orbital parameters corresponding to a marginally unbound orbit ( $e \approx 1$ )—and then consider a range of impact parameters. See Fig. 2 for plots of the NS trajectory for several cases,

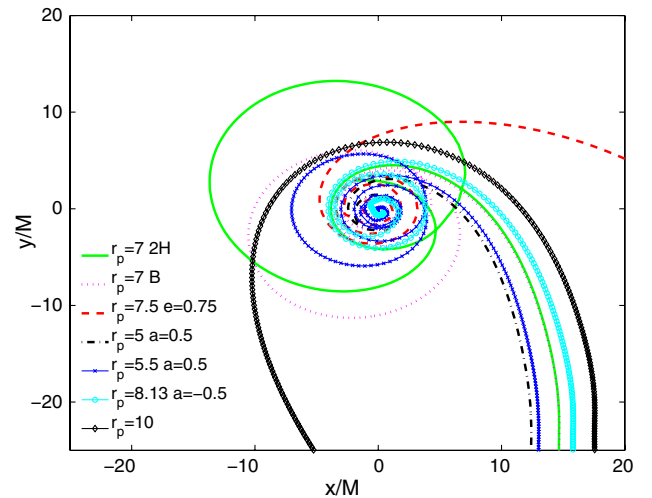


FIG. 2 (color online). Trajectories of the NS center-of-mass for various simulations. The  $r_p = 7.0$  with 2H EOS,  $r_p = 7.0$  with B EOS, and  $r_p = 5.5$   $a = 0.5$  (HB EOS) both undergo a close-encounter followed by a short elliptic orbit before merging. Note that while in both the  $r_p = 7.0$ -cases the NS approaches the BH on essentially the same orbit, the dynamics around the close-encounter and subsequent orbits are very different due to EOS effects (see Sec. IV C). The  $r_p = 10$  (HB EOS) undergoes a long-period elliptical orbit following the initial periastris passage. The remainder of the cases shown merge on the first encounter while displaying various degrees of whirling behavior.

and Fig. 3 for snapshots of the rest-mass density at select times illustrating aspects of the matter dynamics.

#### IV. RESULTS

Varying the parameters as discussed in the previous section, there is much degeneracy in the qualitative features that arise (which will need to be addressed in future studies investigating extraction of source properties from GW and EM observations). This is essentially because the leading-order source of the variability is rooted in the following two properties of the system: (a) the NS radius, varied by altering the EOS (as the NS mass is fixed in this study), (b) the location of the innermost stable orbit (ISO) varied by changing the spin of the BH or the eccentricity of the encounter. For equatorial geodesics on a black hole background, the ISOs asymptote to circular orbits, though these should not be confused with the innermost *stable* circular orbit (at  $r = 6M$  in Schwarzschild), or ISCO. The circular orbits (in the range  $r = 3M$  to  $6M$  in Schwarzschild) associated with the ISOs with nonzero eccentricity are *unstable*, and under infinitesimal perturbation their noncircular nature is manifest in the form of zoom-whirl behavior [67]. Specifically, depending upon the size of the perturbation, the geodesic will undergo a number of near circular orbits (the “whirls”), followed either (depending upon the sign of the perturbation) by a plunge into the BH or by a single near-elliptical orbit (the “zoom”), and in the latter case the motion repeats. Away

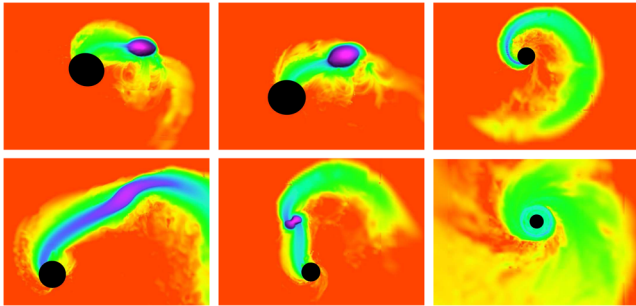


FIG. 3 (color online). Rest-mass density in the equatorial plane from various BH-NS simulations, left to right, top to bottom: (1) the BH and NS undergoing a close-encounter ( $t = 242M$ ,  $r_p = 7.0$ , B EOS), (2) the NS undergoing a whirling-phase before merging ( $t = 269M$ ,  $r_p = 8.13$ ,  $a = -0.5$ ), (3) the NS stretched into a long tidal stream during merger ( $t = 506M$ ,  $r_p = 7.5$ ,  $e = 0.75$ ), (4) a mass-transfer episode ( $t = 292M$ ,  $r_p = 7.0$ , 2H EOS), (5) towards the end of a mass-transfer episode during the NS’s first periapsis passage ( $t = 272M$ ,  $r_p = 5.5$ ,  $a = 0.5$ ), and (6) a nascent accretion disk ( $t = 388M$ ,  $r_p = 5$ ,  $a = 0.5$ ). Recall that  $r_p$  is reported in units of total mass  $M$ . The color scale is logarithmic from  $10^{-6}$  to 1 times the initial maximum density ( $\rho_{\max} = 8.3(3.7, 9.8) \times 10^{14}$  g cm $^{-3}$  for the HB (2H, B) EOS). The BH is roughly the same coordinate size (with diameter  $\approx 3M$ ) in all panels, which can be used to infer the relative scale of each snapshot.

from the geodesic limit there is still an effective ISO, where qualitatively similar behavior occurs [68], though radiation reaction will eventually drive the system to a merger for all bound systems.

In terms of the gravitational dynamics, the closer the periapsis is to the ISO, the more whirling that occurs, resulting in enhanced GW emission and more rapid evolution of effective orbital parameters. Regarding the matter dynamics, the ISO is essentially the “event horizon” for fluid elements following geodesics, or being close to geodesic. What this implies is on a close-encounter, if the NS is not disrupted and the periapsis of the orbit is within the ISO a merger will result and the entire NS will fall into the BH. If the NS is disrupted, following the essentially Newtonian redistribution of angular momentum that results, fluid elements within an ISO corresponding to their effective eccentricity will immediately plunge into the BH while the rest will either move out onto eccentric orbits to later fall back onto an accretion disk or be ejected from the system. If the majority of the NS mass ends up outside the ISO following disruption, once it moves beyond the tidal-disruption zone there will be sufficient self-gravity for the material to re-coalesce into a NS core. Similarly, in a partial disruption where only the outer layers are stripped from the NS, some stripped material will accrete into the BH, some back onto the NS, and a portion will be flung out unbound.

In the following subsections, we break down the discussion of phenomenology of the encounters by first summarizing the results from the base case presented in [10] (Sec. IV A), then describe in turn what happens when spin (Sec. IV B), EOS (Sec. IV C), and eccentricity (Sec. IV D) are changed relative to the base case. In order to have some intuitive understanding of why the changes have the effects they do, it is useful to keep the above discussion in mind. This can also allow one to anticipate what would happen if parameters we are not altering here are changed, for example, the BH or NS mass.

##### A. Zero-spin survey with HB EOS

Here we summarize the results obtained for simulations with an initially nonspinning BH and a NS with the HB EOS (see [10] for more details). We considered a range of periapsis separations from  $r_p/M = 5.0$  to 15 (i.e., 50 to 150 km). Henceforth, we will consider  $r_p$  to be normalized by  $M$ . In all of these cases, sufficient energy is carried away by GWs to result in a bound system. Our simulations exhibit three types of behavior: (1) a direct plunge ( $r_p = 5.0, 5.83, 6.67, 6.81$ ); (2) following the initial periapsis passage, a single elliptical orbit and then a plunge ( $r_p = 6.95, 7.22, 7.5$ ); and (3) following the initial periapsis passage, a long-period elliptical orbit ( $r_p = 8.75, 10.0, 12.5, 15.0$ ). For the latter group (and the high-resolution  $r_p = 7.5$  run), we do not simulate the entire orbit since the length of such simulations would make them very

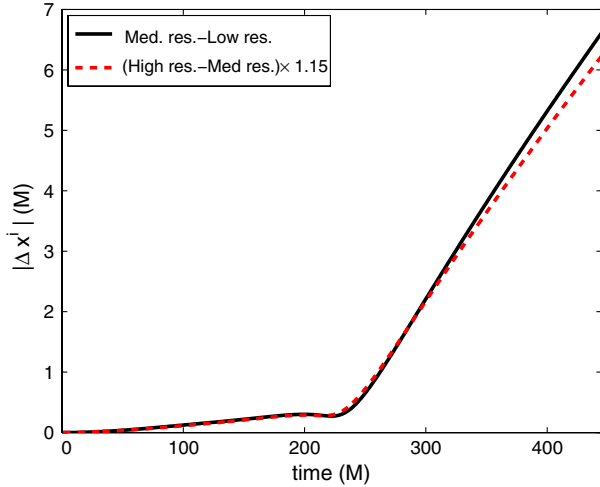


FIG. 4 (color online). Convergence of the NS trajectory for the  $r_p = 10$ ,  $a = 0$ -case (see Sec. IV A). What is plotted is the magnitude of the difference in the center of rest-mass position of the NS between the low and medium-resolution runs, and between the medium and high-resolution runs scaled assuming second-order convergence. The close-encounter occurs near  $t = 230M$ , where the largest “perturbation” of the orbit due to truncation error happens; the relatively large growth of the difference in trajectories following this is mostly just a reflection of this change in the orbital parameters that occurred around periaapsis.

computationally expensive,<sup>1</sup> and we focus on the burst of GWs associated with the first periaapsis passage. For one case in each class ( $r_p = 5.0, 7.5, 10.0$ ) we performed a convergence study which showed approximately second-order convergence and allowed us to perform a Richardson extrapolation to estimate errors in the resulting GWs. To give further indication of the truncation error in these runs, in Fig. 4 we plot the error in the trajectory of the NS in a fly-by case  $r_p = 10$  (see Fig. 2 for the medium resolution trajectory). The GW energy and angular momentum emitted (including extrapolated values from the resolution studies) as well as the disk properties of those cases followed through merger are summarized in Table I. Table II shows the spin of the post-merger BH (for this base set of runs as well as the subsequent parameter survey) for the cases we followed through merger. As the threshold in  $r_p$  dividing (1) and (2) is approached there is a dramatic enhancement in the gravitational energy and angular momentum released during the close-encounter.

<sup>1</sup>For example, based on an estimate using the emitted GWs and assuming a Newtonian orbit the  $r_p = 8.75$  case will undergo another close-encounter after  $\sim 7000M$ , which would take 2–3 months of wall clock time to simulate at medium resolution (while the larger  $r_p$  cases will take even longer). Though such long runs are not unheard of, we chose to use our limited computational resources to explore a greater number of parameters.

The amount of material remaining after merger, which could potentially form an sGRB-powering accretion disk also depends significantly on impact parameter. Below the threshold dividing (1) and (2), there is a sizable amount of remaining material in excess of 20% in the  $r_p = 6.81$  case. In most cases  $\approx 50\%$  of the material is unbound. A simple numerical estimate of the fallback time for the bound material based on when the elliptic orbit will return to the accretion disk shows the characteristic  $t^{-5/3}$  scaling [69].

## B. Effects of black hole spin

As expected from Kerr geodesics, prograde BH spin results in a smaller critical-impact parameter below which the NS merges with the BH on the first encounter than in the nonspinning case; the converse is expected for cases with retrograde initial BH-spin. For the cases with initial BH-spin  $a = 0.5$  (top of Table III), only the  $r_p = 5.0$  case merges on the first encounter while  $r_p = 5.5, 6.0$ , and  $6.25$  go back out on a short elliptic orbit before merging. The  $r_p = 7.5$  and  $10.0$  cases go out on a long elliptic orbit after the initial periaapsis passage, and we did not follow these through merger. For the  $r_p = 5$  case, we also performed convergence tests in order to estimate truncation error for a spinning BH where the effective ISO is closer to the BH. From this we compute Richardson extrapolated values for the energy and angular momentum of the resulting GW as well as for the amount of matter left over post-merger; these values are reported in the table. In Fig. 5 we also show the amount of rest-mass exterior to the BH horizon as a function of time and resolution for this case.

One important consequence of the reduced critical-impact parameter in the prograde case is that around this threshold the tidal forces on the NS are greater and the resulting accretion disks consequently larger. Even more striking, the enhanced tidal interaction can lead to significant mass transfer from the NS to the BH even in nonmerger close-encounters, as, for example, with the  $r_p = 5.5$ ,  $a = 0.5$  case. Here the NS becomes highly distorted and loses approximately 16% of its mass to the BH (see Fig. 6). However, a compact (albeit highly distorted) star remains (see Fig. 3 middle, bottom) until it merges with the BH on its second close-encounter.

For the  $a = -0.5$  cases (see bottom of Table III),  $r_p = 5.0, 7.5$ , and  $8.13$  are direct mergers while the  $r_p = 8.28$  case goes through a single elliptic orbit before merging. The  $r_p = 8.44, 8.75$ , and  $10.0$  cases go out on longer elliptic orbits, which we did not follow to completion. Because of the larger critical-impact parameter for merger on the first encounter, there is less tidal disruption and, hence, the accretion disks contain  $\leq 1\%$  of the total NS rest-mass for all the cases followed through merger. However, this also means that the BH and NS can undergo more whirling behavior in the critical regime before

TABLE I. Disk properties and GW energy and angular-momentum losses for an initially hyperbolic ( $e \approx 1$ ) encounter of a zero-spin BH and NS with HB EOS. Dashed entries correspond to cases that merge during the first encounter, and hence have no “first periapsis”; dotted entries correspond to binaries that were only evolved through first periapsis passage.

$r_p$	$M_0/M_0(t=0)^a$	$M_{0,u}/M_0(t=0)^b$	$\tau_{\text{acc}}$ (ms) <sup>c</sup>	First periapsis <sup>d</sup>		Total <sup>e</sup>	
				$\frac{E_{\text{GW}}}{M} \cdot 10^2$	$\frac{J_{\text{GW}}}{M^2} \cdot 10^2$	$\frac{E_{\text{GW}}}{M} \cdot 10^2$	$\frac{J_{\text{GW}}}{M^2} \cdot 10^2$
5.00	0.005 <sup>g</sup>	0.0	25	-	-	0.67(0.87) <sup>f</sup>	4.14(4.86) <sup>f</sup>
6.67	0.107	0.056	130	-	-	1.29	9.10
6.81	0.221	0.101	40	-	-	1.19	9.60
6.95	0.018	0.003	47	0.697	7.33	1.65	13.9
7.22	0.013	0.001	16	0.358	4.48	1.18	10.2
7.50	0.009	0.003	7.6	0.242(0.147) <sup>f</sup>	3.44(2.46) <sup>f</sup>	1.03	44.7
8.75	...	...	...	0.073	1.58	...	...
10.0	...	...	...	0.033(0.027) <sup>f</sup>	0.97(0.88) <sup>f</sup>	...	...
12.5	...	...	...	0.011	0.46	...	...

<sup>a</sup>Rest-mass remaining outside the BH shortly ( $\sim 50M$ ) after the end of merger, normalized by the initial total rest-mass.

<sup>b</sup>Unbound rest-mass estimated, using local fluid velocities and assuming a stationary metric.

<sup>c</sup>Rough *initial* accretion time scale ( $\tau_{\text{acc}} = M_0/\dot{M}_0$ ) evaluated shortly after merger.

<sup>d</sup>Energy and angular momentum lost to GWs during the first close-encounter.

<sup>e</sup>Total GW energy and angular-momentum losses for cases which were followed through merger.

<sup>f</sup>Results are from medium-resolution runs; values in parentheses are Richardson-extrapolated estimates using low and high resolutions, where available. Note that the relatively large error for  $r_p = 7.5$  (and to a lesser extent  $r_p = 5, 10$ ) is due in part to truncation error altering the actual periapsis by a small amount, and in this regime the GW emission is highly sensitive to binary separation (Fig. 12).

<sup>g</sup>For the  $r_p = 5$  case,  $M_0/M_0(t=0)$  was the same at the three resolutions to within  $\approx 5 \times 10^{-4}$ ; however, for such low disk masses we expect systematic effects, e.g. the numerical atmosphere to be important.

merger. This is especially evident in the waveform for the nearer threshold merger case of  $r_p = 8.13$ ,  $a = -0.5$  as shown in Fig. 10. The gravitational wave signal shows several cycles of almost constant amplitude and frequency, indicative of a nearly circular orbit. Compared to the near-threshold nonspinning case ( $r_p = 6.81$ , also shown in Fig. 10), this whirling period is much more pronounced in the waveform.

### C. Effects of equation of state

We consider the B EOS, which is softer than the HB, and the 2H EOS, which is stiffer. Though the different EOSs have only a slight effect on the critical-impact parameter, they can have a dramatic effect on the near-threshold behavior. For the B EOS, we chose four different impact parameters, (see bottom of Table IV): direct mergers  $r_p = 5.0$  and  $6.25$ ;  $r_p = 7.0$  (after periapsis passage, a

TABLE II. Post-merger BH spin (dimensionless) for various initial conditions. Also shown is the effective spin  $a_{\text{eff}}$  used in the model described in Sec. V and calculated from initial conditions using (3).

$a = 0$ HB EOS								
$r_p$	5.00	6.67	6.81	6.95	7.22	7.50		
$a_{\text{final}}$	0.49 <sup>a</sup>	0.45	0.37	0.47	0.50	0.50		
$a_{\text{eff}}$	0.40	0.46	0.47	0.47	0.48	0.49		
$a = 0.5$				$a = -0.5$				
$r_p$	5.00	5.50	6.00	6.25	5.00	7.50	8.13	8.28
$a_{\text{final}}$	0.74	0.71	0.71	0.70	0.16	0.25	0.22	0.24
$a_{\text{eff}}$	0.72	0.74	0.77	0.77	0.08	0.17	0.19	0.19
2H EOS			B EOS					
$r_p$	5.00	6.75	7.00		5.00	6.25	7.00	
$a_{\text{final}}$	0.50	0.29	0.33		0.48	0.52	0.48	
$a_{\text{eff}}$	0.40	0.46	0.47		0.40	0.45	0.47	
$e = 0.75$								
$r_p$	7.50	7.81						
$a_{\text{final}}$	0.44	0.49						
$a_{\text{eff}}$	0.46	0.47						

<sup>a</sup> $a_{\text{final}} = 0.49 \pm 0.01$

TABLE III. Disk properties and GW energy and angular-momentum losses for an initially hyperbolic ( $e \approx 1$ ) encounter of a BH with spin  $a = \pm 0.5$  and NS with HB EOS.

$r_p$	$M_0/M_0(t=0)^a$	$M_{0,u}/M_0(t=0)^b$	$\tau_{\text{acc}}$ (ms) <sup>c</sup>	First periaapsis <sup>d</sup>		Total <sup>e</sup>	
				$\frac{E_{\text{GW}}}{M} \cdot 10^2$	$\frac{J_{\text{GW}}}{M^2} \cdot 10^2$	$\frac{E_{\text{GW}}}{M} \cdot 10^2$	$\frac{J_{\text{GW}}}{M^2} \cdot 10^2$
$a = +0.5$							
5.00	0.165(0.295) <sup>f</sup>	0.021(0.107) <sup>f</sup>	4.8	-	-	1.25(1.41) <sup>f</sup>	7.14(9.04) <sup>f</sup>
5.50	0.174	0.088	40	0.800	7.14	1.40	10.9
6.00	0.181	0.029	26	0.360	4.16	1.53	14.7
6.25	0.080	0.014	33	0.347	4.11	1.29	12.0
7.50	...	...	...	0.104	1.90	...	...
10.0	...	...	...	0.025	0.82	...	...
$a = -0.5$							
5.00	0.007	0.0	36	-	-	0.33	2.32
7.50	0.008	0.0	71	-	-	0.82	5.91
8.13	0.010	0.0	0.12	-	-	1.57	13.7
8.28	0.002	0.0	2.8	0.385	5.12	1.25	12.8
8.44	...	...	...	0.268	3.98	...	...
8.75	...	...	...	0.167	2.85	...	...
10.0	...	...	...	0.052	1.32	...	...

<sup>a</sup>Rest-mass remaining outside the BH shortly ( $\sim 50M$ ) after the end of merger, normalized by the initial total rest-mass.

<sup>b</sup>Unbound rest-mass estimated using local fluid velocities and assuming a stationary metric.

<sup>c</sup>Rough *initial* accretion timescale ( $\tau_{\text{acc}} = M_0/\dot{M}_0$ ) evaluated shortly after merger.

<sup>d</sup>Energy and angular momentum lost to GWs during the first close-encounter.

<sup>e</sup>Total GW energy and angular-momentum losses for cases which were followed through merger.

<sup>f</sup>For the  $r_p = 5$ ,  $a = +0.5$  case, the Richardson-extrapolated value of  $M_{0,u}/M_0(t=0)$  was computed using just the medium and high-resolution results and assuming second-order convergence due to the low amount of unbound material in the low-resolution case.

short elliptic orbit and then merger); and  $r_p = 7.5$ , which we did not follow through its full elliptic orbit after the first close-encounter. The more compact B EOS NS experiences less tidal disruption and forms accretion disks with  $\leq 1\%$  of the total NS rest-mass for all cases followed through merger. For the 2H EOS, we considered five different impact parameters (see top of Table IV): direct

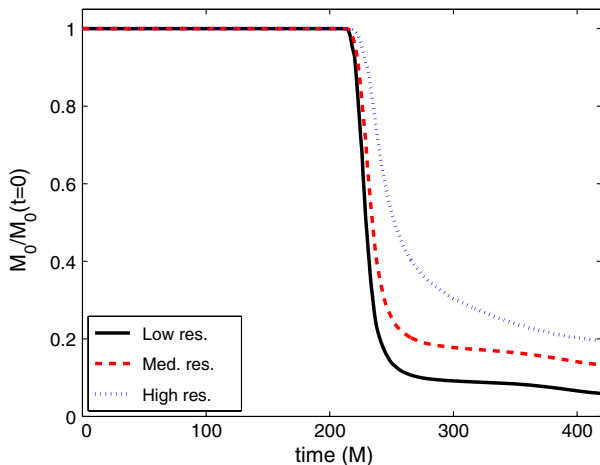


FIG. 5 (color online). Effect of resolution on the disruption and subsequent accretion of NS material, as measured by the total rest-mass exterior to the BH horizon, for the  $r_p = 5$ ,  $a = 0.5$ -case (see Sec. IV B). The amount of rest-mass remaining at late times at the different resolutions is consistent with approximately second-order convergence.

mergers  $r_p = 5.0$  and  $6.75$ ;  $r_p = 7.0$  (after periaapsis passage, a short elliptic orbit and then merger); and  $r_p = 7.25$  and  $7.5$ , which we did not follow through the full elliptic orbit after the first close-encounter.

The less compact 2H EOS NS experiences significant tidal deformation, and for the  $r_p = 6.75$  and  $7.0$  cases there is  $\approx 30\%$  of the NS material leftover post-merger. In the case of  $r_p = 7.0$ , the deformation and tidally-induced oscillations of the NS are especially severe (see Fig. 3, bottom left) and there is a period of significant mass transfer (Fig. 6) from the NS to the BH during the first close-encounter. This is very similar to the  $r_p = 5.5$ ,  $a = 0.5$  case, though more pronounced. For both the 2H EOS and the  $a = 0.5$  with HB EOS simulations no significant mass transfer is found for runs with  $r_p$  slightly above  $7.0$  and  $5.5$ , respectively, so we can use these as an effective measure of the separation  $d_R$  at which the star begins to overflow its Roche lobe. Though the individual values are somewhat higher than expected from Newtonian theory, it predicts a scaling with compaction  $d_R \propto C_{\text{NS}}^{-1}$ , where  $C_{\text{NS}} \equiv M_{\text{NS}}/R_{\text{NS}}$ ; this does approximately hold here since  $C_{\text{HB}}/C_{\text{2H}} = 1.3$ . This ignores any relativistic effects both gauge and physical, the latter including, for example, the effect of BH spin on tidal disruption. In Fig. 7 we show the mass profiles of an isolated star with the 2H and HB EOS. This shows that the outer spherical shell that contains approximately 40% of the NS material accreted into the BH during the first close-encounter for 2H corresponds to a volume containing almost no material in the HB case.

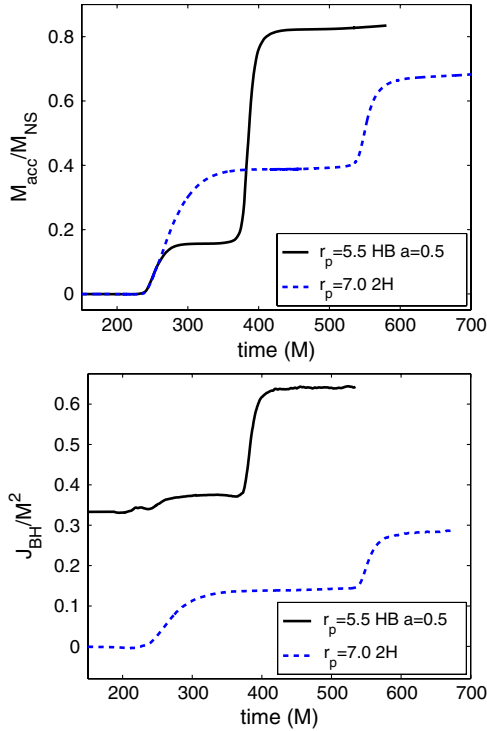


FIG. 6 (color online). *Top*: The amount of rest-mass (normalized to the total rest-mass of the NS) accreted by the BH as a function of time for the  $r_p = 7.0$  2H-case and for the  $r_p = 5.5$ ,  $a = 0.5$  HB-case. In both cases there are two significant episodes of mass transfer. *Bottom*: The angular momentum of the BH horizon in units of the total ADM-mass squared,  $M^2$ , as a function of time for the same two cases.

Again, though we are ignoring the complicated details of mass-transfer dynamics, this is suggestive as to why, for the BH-NS system studied here, there is significant mass transfer for the 2H EOS around  $r_p = 7.0$  but very little for the HB EOS.

Since for the 2H  $r_p = 7.0$  case so much mass is transferred before the merger and there is a strong disruption during merger, the gravitational-wave signal resulting from merger itself is significantly weaker than for other cases (Fig. 10). The full waveform from Fig. 11 also shows that the GW pulse from the fly-by dominates the signal compared to the merger part of the waveform.

Between the initial close-encounter and merger there is also evidence in the GW signal of excited  $f$ -modes within the NS; this was also observed in eccentric-binary NS encounters [11]. Here we give a qualitative account of the stellar dynamics to show that the dominant oscillation is akin to that of an  $f$ -mode of an isolated, perturbed star—a detailed study, aside from the difficulty of applying a perturbative analysis in such a transient and in some cases highly distorted star, is beyond the scope of this study. Figure 8 demonstrates the density and velocity distortions for the  $r_p = 7.0$ , 2H case (right panel) as well as the  $r_p = 6.95$  HB case in which the distortion is less extreme (left panel). The latter bears a particularly strong resemblance to the pure  $l = m = 2$   $f$ -mode flow pattern (see, e.g., Fig. 19 of [70]). In both cases, an animation of the density field seems to suggest a rotating, distorted NS. However, as Fig. 8 demonstrates, the velocity pattern is not one of overall rotation but rather that of an oscillatory mode. Indeed, the circulation theorem should hold to a good approximation in the bulk of the NS material (though there are entropy-generating shocks near the surface). Thus, the

TABLE IV. Disk properties and GW energy and angular-momentum losses for an initially hyperbolic ( $e \approx 1$ ) encounter of a BH with zero-spin and a NS with 2H and B EOS.

$r_p$	$M_0/M_0(t=0)^a$	$M_{0,u}/M_0(t=0)^b$	$\tau_{\text{acc}}$ (ms) <sup>c</sup>	First periapsis <sup>d</sup>		Total <sup>e</sup>	
				$\frac{E_{\text{GW}}}{M} \cdot 10^2$	$\frac{J_{\text{GW}}}{M^2} \cdot 10^2$	$\frac{E_{\text{GW}}}{M} \cdot 10^2$	$\frac{J_{\text{GW}}}{M^2} \cdot 10^2$
2H EOS							
5.00	0.008	0.0	56	-	-	0.58	3.61
6.75	0.278	0.117	18	-	-	0.47	4.65
7.00	0.303	0.149	60	0.387	4.53	0.43	5.41
7.25	...	...	...	0.283	3.90	...	...
7.50	...	...	...	0.200	3.07	...	...
B EOS							
5.00	0.008	0.0	57	-	-	0.60	3.83
6.25	0.008	0.0	64	-	-	0.87	5.63
7.00	0.010	0.001	10	0.718	7.69	1.73	10.7
7.50	...	...	...	0.268	3.72	...	...

<sup>a</sup>Rest-mass remaining outside the BH shortly ( $\sim 50M$ ) after the end of merger, normalized by the initial total rest-mass.

<sup>b</sup>Unbound rest-mass estimated using local fluid velocities and assuming a stationary metric.

<sup>c</sup>Rough initial accretion time scale ( $\tau_{\text{acc}} = M_0/M_0$ ) evaluated shortly after merger.

<sup>d</sup>Energy and angular momentum lost to GWs during the first close-encounter.

<sup>e</sup>Total GW energy and angular-momentum losses for cases which were followed through merger.

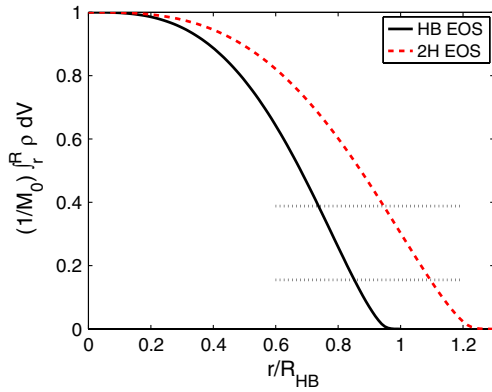


FIG. 7 (color online). The fraction of rest-mass outside a given radius  $(1/M_0) \int_r^R \rho dV$  for an isolated star with the HB or 2H EOS and  $M = 1.35M_\odot$ . Here radius  $r$  is normalized to the radius of the HB star ( $R_{\text{HB}}$ ). The horizontal, dotted-lines indicate the amount of material accreted into the BH during the initial close-encounter for the  $r_p = 5.5$ -case with HB EOS (bottom) and the  $r_p = 7.0$ -case with 2H EOS (top) as shown in Fig. 6.

tidal interaction with the BH would not induce rotation in the usual sense but rather oscillatory modes with rotating patterns. Many such modes are likely to be excited, but the  $l = m = 2$   $f$ -mode seems to dominate. We performed a spherical-harmonic decomposition of the star's rest-mass density  $\rho = \sum C_{lm} Y_{lm}$  at select times and found  $C_{22}$  to be

the largest coefficient next to  $C_{00}$ . We also checked that the perturbation amplitude grows monotonically with radius. For the  $r_p = 6.95$  simulation with the HB EOS  $|C_{22}/C_{00}| \approx 0.01$ – $0.02$  at  $r = 0.4M$  grows to  $|C_{22}/C_{00}| \approx 0.15$ – $0.20$  at  $r = 0.8M$ . Here  $r$  is the radius of the sphere centered on the NS center-of-mass on which the coefficients are calculated. The next largest coefficient  $C_{20}$  is smaller by a factor of  $\approx 2$ . The  $r_p = 7.0$  simulation with the 2H EOS shows similar behavior although the coefficients are somewhat larger with  $|C_{22}/C_{00}| \approx 0.03$  and  $0.25$  at  $r = 0.4M$  and  $0.8M$ , respectively.

We briefly comment on the possible detectability of such an  $f$ -mode excitation in GWs. Such an observation in principle could provide a wealth of information about the structure of the NS, in particular, since  $f$ -mode frequencies are quite sensitive to the EOS (see for example [71]). However, here, (a) the amplitudes are quite low relative to the dominant GW emission (see Fig. 11), (b) for the cases where the largest amplitudes are excited, the initial  $r_p$  is sufficiently small that only a few cycles of waves will be emitted before subsequent merger, limiting the signal-to-noise that could be built up, and (c) the frequency is quite high (above 1 kHz) and thus not in a regime where the AdLIGO-class detectors are very sensitive. Thus, even if there is a sizable population of eccentric merger events as studied here, it is unlikely that any corresponding  $f$ -mode

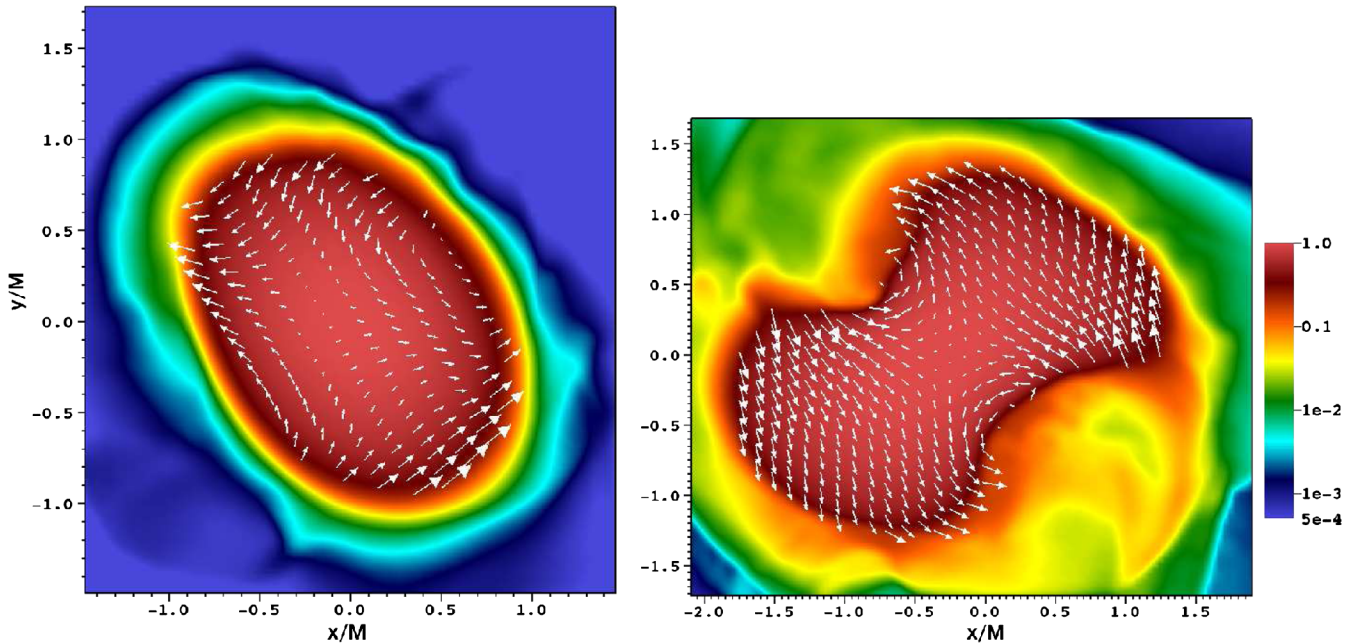


FIG. 8 (color online). NSs exhibiting large-amplitude  $f$ -mode oscillations following the first interaction with the (nonspinning) BH. The cases shown are  $r_p = 6.95$  with the HB EOS at  $t = 341M$  (left) and  $r_p = 7.0$  with the 2H EOS at  $t = 356M$  (for the latter case, see the bottom left-panel of Fig. 3 for a snapshot of the density near the time of closest approach to the BH when this large oscillation is excited). The color map shows the rest-mass density in the equatorial plane on a logarithmic scale, normalized to the instantaneous maximum density. The arrows show the velocity in the NS center-of-mass frame. The longest velocity arrows correspond to velocity magnitudes  $0.084$  (left) and  $0.17$  (right). Though the two cases have similar periastron radii, the lower compaction in the 2H-case leads to a much stronger tidal interaction and an  $f$ -mode, which shows nonlinear characteristics.

TABLE V. Disk properties and GW energy and angular-momentum losses for an initially eccentric  $e = 0.75$  encounter of a zero-spin BH with a NS with HB EOS.

$r_p$	$M_0/M_0(t=0)^a$	$M_{0,u}/M_0(t=0)^b$	$\tau_{\text{acc}} \text{ (ms)}^c$	First periapsis <sup>d</sup>		Total <sup>e</sup>	
				$\frac{E_{\text{GW}}}{M} \cdot 10^2$	$\frac{J_{\text{GW}}}{M^2} \cdot 10^2$	$\frac{E_{\text{GW}}}{M} \cdot 10^2$	$\frac{J_{\text{GW}}}{M^2} \cdot 10^2$
7.50	0.109	0.062	32	-	-	1.47	13.6
7.81	0.007	0.001	7.1	0.410	5.25	1.58	16.1
8.13	...	...	...	0.248	3.67	...	...
8.75	...	...	...	0.125	2.34	...	...
10.0	...	...	...	0.049	1.28	...	...

<sup>a</sup>Rest-mass remaining outside the BH shortly ( $\sim 50M$ ) after the end of merger, normalized by the initial total rest-mass.

<sup>b</sup>Unbound rest-mass estimated, using local fluid velocities and assuming a stationary metric.

<sup>c</sup>Rough *initial* accretion time scale ( $\tau_{\text{acc}} = M_0/M_0$ ) evaluated shortly after merger.

<sup>d</sup>Energy and angular momentum lost to GWs during the first close-encounter.

<sup>e</sup>Total GW energy and angular-momentum losses for cases which were followed through merger.

excitation will be observed with the current generation of GW detectors.

#### D. Bound eccentric evolution

Finally, we simulated binaries where the BH and NS have initial-orbital parameters corresponding to a bound orbit with  $e = 0.75$  for a range of values of  $r_p$ . These simulations can be viewed as corresponding to systems that have already become bound through one or more close-encounters and lost some of their initial eccentricity. In practice, the length of such evolutions would be very computationally expensive to follow in full. Of the impact parameters considered (see Table V),  $r_p = 7.5$  is the only direct-plunge, and  $r_p = 7.81$  is the only case we followed past periapsis passage to merge on the second close-encounter. For the remaining cases ( $r_p = 8.13, 8.75,$  and  $10.0$ ), we only followed partially through their elliptic orbits after the first close-encounter. The threshold for merger on the first encounter moves out slightly in this case as an appeal to geodesics in Schwarzschild would suggest. In Fig. 9, we plot the gravitational waveforms from two fly-by close-encounters  $r_p = 8.13$  and  $10.0$ . In addition, we fit the expected waveform according to a Newtonian-order quadrupole approximation [14,65,72] (NQA) to our numerical results by multiplying by an overall factor. As found in [10] and in our other simulations here for the marginally unbound case, though the shape of the waveforms agree quite well, the numerical results exhibit a significant amplitude enhancement that is larger the closer one gets to the threshold for merger during the close-encounter. In addition, from Fig. 10 we can see that the near-threshold merger waveform shows more evidence of whirling than the initially unbound case.

#### V. EVOLUTION OF ORBITAL PARAMETERS

As noted in [10], there is a dramatic enhancement in gravitational-wave energy and angular momentum emitted in a BH-NS close-encounter that occurs as the threshold for merger on the first encounter is approached. In this section,

we will attempt to explain this enhancement by analogy to the zoom-whirl orbits in Kerr spacetimes, and extrapolate this behavior to close-encounters with different eccentricities and spins. Then we will use these results to approximate the evolution of orbital parameters for BH-NS systems undergoing a series of close-encounters.

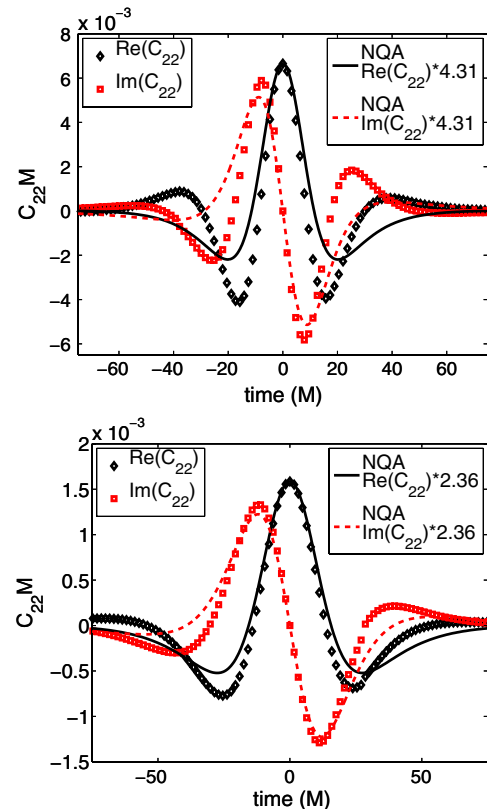


FIG. 9 (color online). The real and imaginary components (black diamonds and red squares) of the  $l = 2, m = 2$  spherical-harmonic of  $r\Psi_4$  for  $e = 0.75$  and  $r_p = 8.125$  (top) and  $r_p = 10$  (bottom). For comparison the NQA analytical results are shown multiplied by an overall factor so that the magnitude and phase match at peak ( $t = 0$ ).

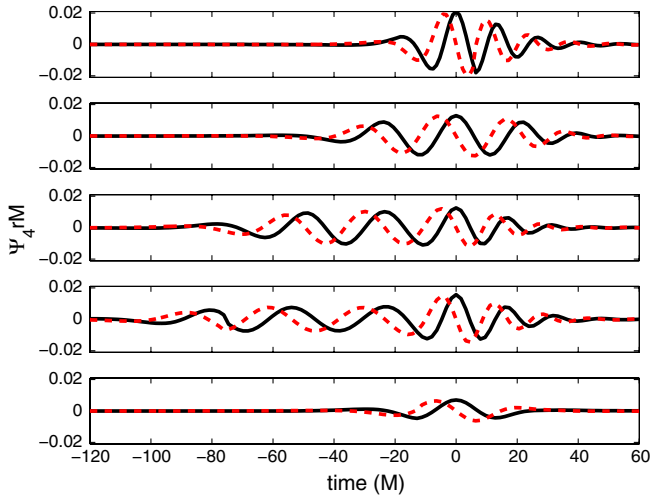


FIG. 10 (color online). The real and imaginary components (solid, black-lines and red, dotted-lines) of  $\Psi_4$  on the  $z$ -axis (perpendicular to the orbital plane) during merger for the following cases (top to bottom):  $r_p = 5$ , HB;  $r_p = 6.81$ , HB;  $r_p = 7.5$ ,  $e = 0.75$ , HB;  $r_p = 8.13$ ,  $a = -0.5$ , HB; and  $r_p = 7.0$ , 2H (see Fig. 11 for the full signal). The waveforms are aligned so that the peak occurs at  $t = 0$  with zero phase.

### A. Zoom-whirl enhancement

As discussed in the previous section and as can be seen in Fig. 12, though different values of initial spin or eccentricity may shift the critical value of  $r_p$ , which we shall call  $r_c$  at which the NS merges with the BH during a first encounter; for all the cases considered there is a

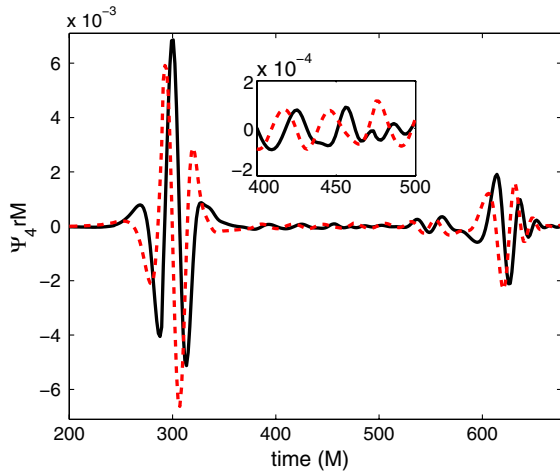


FIG. 11 (color online). The real and imaginary components (solid, black-lines and red, dotted-lines) of  $\Psi_4$  on the  $z$ -axis (perpendicular to the orbital plane) at  $r = 70M$  for the  $r_p = 7.0$  2H simulation. The large burst at  $t \approx 300M$  comes from the initial fly-by, where the NS becomes extremely distorted (Fig. 3) and loses a significant portion of its mass (Fig. 6). The smaller pulse at  $t = 600M$  comes from the merger. In between, there is a smaller component of the signal coming from the tidally induced oscillation of the NS.

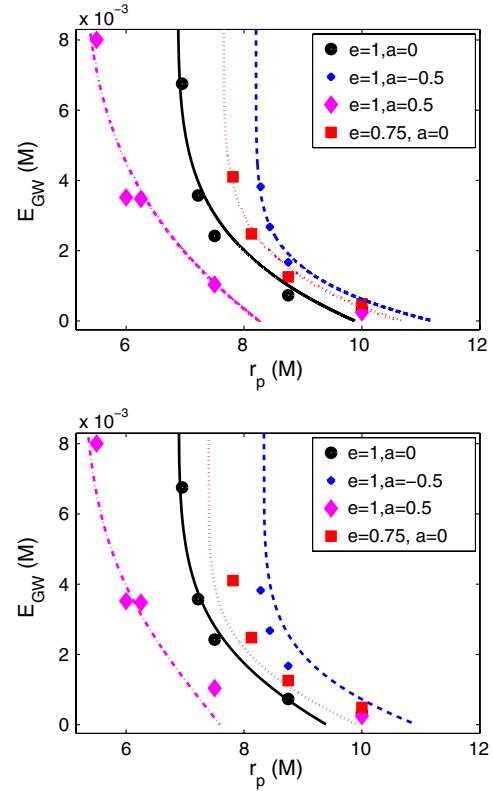


FIG. 12 (color online). *Top*: Energy lost to GWs during the initial close-encounter (i.e. excluding merger) as a function of  $r_p$  for initial BH-spin  $a = 0, -0.5$ , and  $0.5$  and for initial eccentricity  $e = 1$  and  $0.75$ . The functional form  $E_0(1 - (\delta r_p/\Delta)^\gamma)$  (lines) motivated by zoom-whirl dynamics is a fit to the simulation results (points).  $\delta r_p = r_p - r_c$  where  $r_c$  is the threshold value for merger during the encounter.  $E_0$  is the difference in energy between a quasicircular orbit and an  $e \approx 1$  ( $0.75$ ) orbit, both having  $r_p = r_c$ .  $\Delta$  is the range over which zoom-whirl-like behavior dominates the GW-emission energetics.  $\gamma$  is a parameter that in the geodesic analogue is related to the instability exponent of the corresponding unstable circular orbit, here, we use it as our fitting parameter. We obtain  $\gamma = 0.19, 0.13, 0.25$ , and  $0.16$  for  $(e, a) = (1, 0), (1, -0.5), (1, 0.5)$ , and  $(0.75, 0)$ , respectively. *Bottom*: This shows the same simulation data points as the top figure, though here we use the  $e = 1, a = 0$  case (solid, black points) to determine the free parameters for the method described in the text to extrapolate the values of  $r_c$  and  $\gamma$  to the other three cases.

significant enhancement in the energy of the gravitational waves emitted as this threshold is approached. This can be understood by analogy to the zoom-whirl orbits in Kerr spacetimes. As the BH-NS approaches the critical-impact parameter, it is closer and closer to the unstable orbit dividing plunging and nonplunging orbits and will, therefore, exhibit more and more whirling behavior. Though the effect is most dramatic near threshold, this zoom-whirl analog is a way to understand the significant enhancements over the NQA predictions that persist till  $r_p \approx 10$  (see Fig. 4 in [10]). This motivates a fit to the GW energy

emitted in a whirling close-encounter with the functional form (see Fig. 12),

$$E_{\text{GW}} = E_0(1 - (\delta r_p/\Delta)^\gamma), \quad (2)$$

where  $\delta r_p = r_p - r_c$ ,  $E_0$  is the difference in energy between a quasicircular orbit and an eccentricity  $e$  orbit both with  $r_p = r_c$ ,  $\Delta$  is the range over which zoom-whirl-like behavior dominates the GW-emission energetics, and  $\gamma$  is a parameter that in the geodesic analogue is related to the instability exponent of the corresponding unstable circular orbit. Given the limited number of points we have, we choose to use  $\gamma$  as our single-fitting parameter. We set  $r_c$  to the average of the closest sub and supercritical values of  $r_p$  from the simulations. We choose  $\Delta = 3$  by inspection so that values of  $r_p$  outside this range are well-approximated by the NQA model. Certainly, in future work once more data points are available it would be preferable to more systematically fit to the other parameters as well, and refine the model.

The top panel of Fig. 12 shows this fitting performed individually to each set  $(e, a)$  of simulations run. We should note that due to limited computational resources, we have not been able to perform this fitting at multiple resolutions in order to be able to estimate the effect of truncation error on  $\gamma$ . However, due to the sensitivity of  $E_{\text{GW}}$  on  $r_p$  that can be seen in Fig. 12, one would expect that the truncation error in these values will be dominated by the resolution dependence of  $r_c$  as opposed to the error in  $\gamma$ . In the remainder of this section we will use the data from the  $e \approx 1$ ,  $a = 0$  set to calibrate geodesic-inspired extensions to arbitrary values of  $(e, a)$ , which can then be compared to the other three sets of simulation data (bottom panel of Fig. 12) to test how well this extrapolation works.

To extend this model to different values of eccentricity  $e$  and BH spin  $a$ , we assume that the dependency of  $r_c$  and  $\gamma$  on these values is the same as in the geodesic case on a Kerr background. We will use  $a_{\text{eff}}$  to refer to the effective spin parameter we use in the Kerr formulas. For better correspondence with the Kerr spacetime, we want to take  $a_{\text{eff}}$  to be the approximate spin of the BH that would form if a merger occurred. We do this rather than use the initial spin of the BH based on results from [68], which suggest that far from the geodesic limit the total angular momentum of the binary is more important than the BH spin. We estimate  $a_{\text{eff}}$  using

$$a_{\text{eff}} = a_0 \frac{\sqrt{(1+e)r_p}}{\sqrt{2r_{c0}}} + a(M_{\text{BH}}/M)^2, \quad (3)$$

where  $M_{\text{BH}}$ ,  $a$ ,  $r_p$ , and  $e$  are the initial BH-mass, initial BH-spin, periapsis, and eccentricity, respectively, of the encounter for which we want to compute for an  $a_{\text{eff}}$ , and  $a_0 \approx 0.5$  is the final spin measured from the  $e \approx 1$ ,  $a = 0$ ,  $r_p = r_{c0} \approx 6.9$  simulation. In Table II, we show how  $a_{\text{eff}}$  compares to the final BH-spins in the simulations that we followed through merger. This simple formula based on the

total angular momentum of the system does not attempt to capture any of the complications due to differences in matter dynamics or gravitational radiation between the different cases, and as can be seen does not always capture the trends with  $r_p$  seen in the simulations. We use  $a_{\text{eff}}$  because it has a simple motivation, and it does a decent job of estimating the final BH-spin for the purposes of this model. This allows us to extend this model to other values eccentricity  $e$  and BH-spin  $a$  that were not simulated.

Recall that for equatorial geodesics with eccentricity  $e$  in Boyer-Lindquist coordinates with BH-spin parameter  $a$ , there is a value for the periapsis that corresponds to a marginally unstable orbit  $r_c^{\text{BL}}(e, a)$ . It can be found by solving the equation (see, for example, [73])  $(r_c^{\text{BL}})^2 = (J - aE)^2(1 + e)/(3 - e)$ , where  $E$  and  $J$  are the orbit's specific energy and angular momentum, respectively. For our model, we assume that  $r_c(e, a_{\text{eff}}) \propto r_c^{\text{BL}}(e, a_{\text{eff}})$ , and we fit the proportionality constant using our numerical results for  $e \approx 1$ ,  $a = 0$ .

The instability exponent for unstable circular orbits in Boyer-Lindquist coordinates is given by [68,74]

$$\gamma^{\text{BL}}(e, a) = \frac{r}{2\pi} \left[ 3r^2 D + \frac{4M}{\omega^2} (rR^2 \omega^2 - 4Ma\omega - r + 2m) \right]^{-1/2}, \quad (4)$$

where  $R = r^2 + a^2(1 + 2M/r)$ ,  $D = r^2 + a^2 - 2Mr$ ,  $\omega = M/(Ma \pm \sqrt{Mr^3})$  ( $\pm$  for prograde and retrograde, respectively), and we set  $r = r_c^{\text{BL}}(e, a)$ . Again, we assume that  $\gamma(e, a_{\text{eff}}) \propto \gamma^{\text{BL}}(e, a_{\text{eff}})$  and fit the proportionality constant using our numerical results for  $e \approx 1$ ,  $a = 0$ . For the angular momentum lost to gravitational waves in a close-encounter we assume a similar expression

$$J_{\text{GW}} = J_0(1 - (\delta r_p/\Delta)^\gamma), \quad (5)$$

where again  $J_0$  is the difference in angular momentum of a quasicircular orbit and an eccentricity  $e$  orbit evaluated at the same separation  $r_p$ .

This simple prescription for estimating gravitational-wave energy and angular-momentum loss has some obvious limitations. We are extrapolating the critical-impact parameter and instability exponent based on a Kerr spacetime to a BH-NS spacetime that is dynamic and nonperturbative. We are also ignoring tidal effects or dependence on EOS in this model. Nevertheless, in Fig. 12, we compare how closely this predicted scaling with spin and eccentricity matches that from simulation results. Given its simplicity, as well as the numerical error in these results, this model does a satisfactory job of capturing the trends in these scalings.

## B. Systems undergoing multiple close-encounters

The enhanced GW energy and angular-momentum losses during a close-encounter for a given  $r_p$  result in

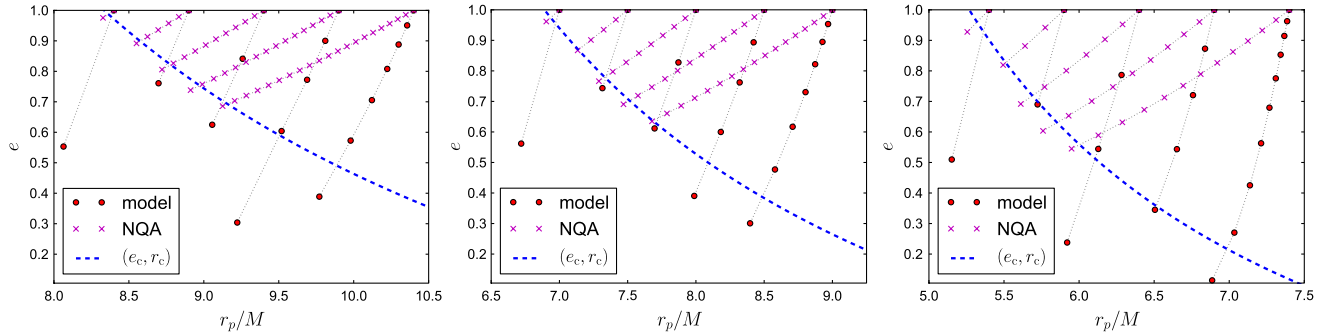


FIG. 13 (color online). The evolution of the eccentricity and periastron separation of various 4:1 mass ratio BH-NS binaries that begin marginally unbound and undergo a series of close-encounters (large red points) before merging. For comparison, we also plot the results using the NQA expressions from [14,65] (magenta  $x$ 's). We also plot the critical eccentricity for a given  $r_p$  for a close-encounter to result in merger (blue, dotted-line). Hence, the points below this curve correspond to merger events. From left to right the plots correspond to an initial BH-spin of  $a = -0.5, 0$ , and  $0.5$ , respectively.

more rapid loss of eccentricity and larger rate of decrease of  $r_p$  of the next encounter. Figure 13 shows approximate trajectories in  $e$  and  $r_p$  for binaries on initially marginally unbound (i.e.  $e = 1 + \epsilon$ ) orbits for a range of initial BH-spin. These results were obtained using the above model for energy and angular momentum lost to GWs and assuming  $e$  and  $r_p$  follow the Newtonian relationship to energy and angular momentum. We approximate these losses as occurring in discrete steps during close-encounters. (This approximation will break down as  $e \rightarrow 0$ .) Trajectories computed with the NQA amplitude and eccentricity-dependence [14,65,72] are also shown in the figure. The NQA execute many more orbits before merger. This clear departure from the NQA prediction at small  $r_p$  due to strong field-GR effects should thus be apparent in the gravitational waveform. This model can also be used to predict approximately the critical-initial impact parameter for the BH-NS system to merge on the second close-encounter, the third close-encounter, and so on. We expect interesting dynamics around each of the thresholds up until the point where the system has undergone enough close-encounters that it circularizes.

## VI. CONCLUSION

We have performed an initial survey of eccentric BH-NS mergers including the effects of black hole spin and varying the NS EOS. Though the limited number of values we considered in this work does not begin to exhaust the parameter space, what is immediately apparent is the strong diversity in the resulting gravitational and matter dynamics. Though we have not yet studied the consequences of this on gravitational-wave detectability and parameter extraction, or possible electromagnetic counterparts, it is clear that the outcome can depend sensitively on the binary parameters and matter EOS.

In order to understand the effects of large eccentricity, these simulations can be compared to the quasicircular BH-NS merger simulations of [38,44], which used the

same piecewise polytrope equations of state. In [44], it was found that for a nonspinning BH and a 3:1-mass ratio, the resulting disk masses were  $0.044$ ,  $0.0015$ , and  $< 10^{-5} M_\odot$  for the 2H, HB, and B EOSs, respectively. Hence, eccentric mergers with certain ranges of impact parameters is one way to achieve significantly larger accretion disks compared to the quasicircular case without BH spin. The effects of BH spin were considered in [38], where for a 4:1-mass ratio and the HB EOS they found disk masses of  $0.024$  and  $0.18 M_\odot$  for BH spins of  $a = 0.5$  and  $0.75$ , respectively, [and even larger values for stiffer EOSs or lower mass ratios]. They also only found a non-negligible amount of unbound material ( $\geq 0.01 M_\odot$ ) only for stiff EOSs like the 2H. Thus, an important characteristic of eccentric mergers is the larger amount of ejected material found for some parameters. This could be a significant source of  $r$ -process elements [30–32], and give rise to EM counterparts, e.g. through nuclear decay of the radioactive  $r$ -process isotopes [8,33]. The amount of energy radiated away in gravitational waves for the quasicircular case is somewhat higher than the values found here (for example,  $E_{\text{GW}} = 1.7\%$  of the total mass for a 4:1 mass ratio, HB EOS, and  $a = 0.5$  in [38]). The gravitational-wave signal is of course completely different for eccentric mergers, which are dominated by bursts from close-encounters or merger of the two compact objects.

Whether dynamical capture BH-NS mergers occur with sufficient frequency in the Universe to constitute a decent event rate for ground-based GW detectors is another question; at the least, failure to observe such events will place constraints on these sources, while if several are observed given the sensitivity of the outcome to properties of the binary, they could be ideal environments to reveal the structure of neutron stars. And again, we should emphasize that excessive fine tuning of parameters is not required for significant variability. Taking the relative velocity at large separations in a typical nuclear-cluster cusp as an example ( $\approx 1000$  km/s), roughly 25% of such encounters will have  $r_p \lesssim 10$ , (following the same line of reasoning discussed

in the introduction for the percentage of direct collisions) corresponding to the cases studied here. Certainly some of the most extreme examples of mass transfer, large accretion disks, or multiple whirl orbits will be rare; perusing Tables I, III, IV, and V will give some idea of the distribution with  $r_p$ . (Recall that the cross section scales linearly with  $r_p$  due to gravitational focusing, and that one would also expect some cases with larger initial  $r_p$  than we followed through merger to exhibit similar variability.) It is not trivial to calculate a transition value of initial  $r_p$  above which the qualitative behavior at late times is described by a quasicircular inspiral, though our study suggests at least a quarter of dynamical-capture binaries will merge with high eccentricity.

For future work, we plan to investigate the detectability of the GW signals from BH-NS mergers that arise from dynamical capture in the strong-field regime. This will complement the first study of such systems presented in [21], in that we intend to focus on the later stages of high-eccentricity mergers, including the merger/ringdown part of the signal. Future work also includes expanding the parameter space to different BH and NS masses, BH-spin orientations, and (as computational resources permit) evolution of systems that exhibit more than two close-encounters before merger. Performing higher-resolutions

simulations will also be important to coming up with a more quantitatively accurate model of the behavior of the BH-NS binary near the threshold for merger during a given close-encounter. Doing so will not only require additional computational resources but a better method for creating initial data describing such eccentric binaries, since the superposition method used here imposes an effective floor on the accuracy that be reached. It would also certainly be interesting to investigate EM counterparts to these events; such simulations would require extensions to the code used here beyond the present GRHD.

## ACKNOWLEDGMENTS

We thank Adam Burrows, John Friedmann, Roman Gold, Janna Levin, Charalampos Markakis, Benjamin Lackey, Sean McWilliams, and Richard O’Shaughnessy for useful conversations. This research was supported by the NSF through TeraGrid resources provided by NICS under Grant No. TG-PHY100053, the Bradley Program (B. C. S.), the NSF Graduate Research Program under Grant No. DGE-0646086 (W. E.), NSF Grant No. PHY-0745779 (F. P.) and Grant No. PHY-1001515 (B. C. S.), and the Alfred P. Sloan Foundation (F. P.). Simulations were also run on the *Woodhen* cluster at Princeton University.

- 
- [1] A. Abramovici, W. E. Althouse, R. W. P. Drever, Y. Gürsel, S. Kawamura, F. J. Raab, D. Shoemaker, L. Sievers, R. E. Spero, K. S. Thorne, R. E. Vogt, R. Weiss, S. E. Whitcomb, and Michael E. Zucker, *Science* **256**, 325 (1992).
  - [2] R. Narayan, B. Paczynski, and T. Piran, *Astrophys. J.* **395**, L83 (1992).
  - [3] N. Gehrels *et al.*, *Nature (London)* **437**, 851 (2005).
  - [4] W. H. Lee, E. Ramirez-Ruiz, and J. Granot, *Astrophys. J. Lett.* **630**, L165 (2005).
  - [5] A. Rau *et al.*, *Publ. Astron. Soc. Pac.* **121**, 1334 (2009).
  - [6] N. Kaiser, in *Society of Photo-Optical Instrumentation Engineers (SPIE) Conference Series*, edited by J. M. Oschmann Jr., Society of Photo-Optical Instrumentation Engineers (SPIE) Conference Series, Vol. 5489 (SPIE Bellingham, WA, (2004), p. 11.
  - [7] P. A. Abell, J. Allison, S. F. Anderson, J. R. Andrew, J. R. P. Angel, L. Armus, D. Arnett, S. J. Asztalos, T. S. Axelrod, and S. Bailey, *et al.* (LSST Science Collaborations), *LSST Science Book, Version 2.0.*, (LSST Corporation, Tuscon, Arizona, 2009).
  - [8] B. D. Metzger and E. Berger, [arXiv:1108.6056v1](https://arxiv.org/abs/1108.6056v1).
  - [9] N. Dalal, D. E. Holz, S. A. Hughes, and B. Jain, *Phys. Rev. D* **74**, 063006 (2006).
  - [10] B. C. Stephens, W. E. East, and F. Pretorius, *Astrophys. J. Lett.* **737**, L5 (2011).
  - [11] R. Gold, S. Bernuzzi, M. Thierfelder, B. Bruegmann, and F. Pretorius, [arXiv:1108.6056v1](https://arxiv.org/abs/1108.6056v1).
  - [12] M. Shibata and K. Taniguchi, *Living Rev. Relativity* **14** 6 (2011).
  - [13] W. H. Press and S. A. Teukolsky, *Astrophys. J.* **213**, 183 (1977).
  - [14] P. C. Peters and J. Mathews, *Phys. Rev.* **131**, 435 (1963).
  - [15] R. M. O’Leary, B. Kocsis, and A. Loeb, *Mon. Not. R. Astron. Soc.* **395**, 2127 (2009).
  - [16] W. H. Lee, E. Ramirez-Ruiz, and G. van de Ven, *Astrophys. J.* **720**, 953 (2010).
  - [17] J. Grindlay, S. Portegies Zwart, and S. McMillan, *Nature Phys.* **2**, 116 (2006).
  - [18] R. Salvaterra, A. Cerutti, G. Chincarini, M. Colpi, C. Guidorzi, and P. Romano, *Mon. Not. R. Astron. Soc.* **388**, L6 (2008).
  - [19] D. Guetta and L. Stella, *Astron. Astrophys.* **498**, 329 (2009).
  - [20] K. Belczynski, M. Dominik, T. Bulik, R. O’Shaughnessy, C. Fryer, and D. E. Holz, *Astrophys. J. Lett.* **715**, L138 (2010).
  - [21] B. Kocsis and J. Levin, [arXiv:1109.4170v1](https://arxiv.org/abs/1109.4170v1).
  - [22] J. Abadie, B. P. Abbott, R. Abbott, M. Abernathy, T. Accadia, F. Acernese, C. Adams, R. Adhikari, P. Ajith, and B. Allen *et al.*, *Classical Quantum Gravity* **27**, 173001 (2010).
  - [23] E. Berger, *Astrophys. J.* **722**, 1946 (2010).
  - [24] R. P. Church, A. J. Levan, M. B. Davies, and N. Tanvir, *Mon. Not. R. Astron. Soc.* **413**, 2004 (2011).
  - [25] J. D. M. Dewi, P. Podsiadlowski, and O. R. Pols, *Mon. Not. R. Astron. Soc.* **363**, L71 (2005).

- [26] J.P. Norris, N. Gehrels, and J.D. Scargle, *Astrophys. J.* **735**, 23 (2011).
- [27] W.F. Domainko, *Astron. Astrophys.* **533**, L5 (2011).
- [28] T.A. Thompson, *Astrophys. J.* **741**, 82 (2011).
- [29] Linqing Wen, *Astrophys. J.* **598**, 419 (2003).
- [30] J.M. Lattimer and D.N. Schramm, *Astrophys. J. Lett.* **192**, L145 (1974).
- [31] S. Rosswog, F.K. Thielemann, M.B. Davies, W. Benz, and T. Piran, [arXiv:astro-ph/9804332v2](https://arxiv.org/abs/astro-ph/9804332v2).
- [32] Li-X. Li and B. Paczynski, *Astrophys. J.* **507**, L59 (1998).
- [33] B.D. Metzger, G. Martínez-Pinedo, S. Darbha, E. Quataert, A. Arcones, D. Kasen, R. Thomas, P. Nugent, I.V. Panov, and N.T. Zinner, *Mon. Not. R. Astron. Soc.* **406**, 2650 (2010).
- [34] C.F. Gammie, S.L. Shapiro, and J.C. McKinney, *Astrophys. J.* **602**, 312 (2004).
- [35] J.M. Miller, M.C. Miller, and C.S. Reynolds, [arXiv:1102.1500v1](https://arxiv.org/abs/1102.1500v1).
- [36] Z.B. Etienne, Y.T. Liu, S.L. Shapiro, and T.W. Baumgarte, *Phys. Rev. D* **79**, 044024 (2009).
- [37] F. Foucart, M.D. Duez, L.E. Kidder, and S.A. Teukolsky, *Phys. Rev. D* **83**, 024005 (2011).
- [38] K. Kyutoku, H. Okawa, M. Shibata, and K. Taniguchi, *Phys. Rev. D* **84**, 064018 (2011).
- [39] S. Chawla M. Anderson, M. Besselman, L. Lehner, S.L. Liebling, P.M. Motl, and D. Neilsen, *Phys. Rev. Lett.* **105**, 111101 (2010).
- [40] J.S. Read, C. Markakis, M. Shibata, K. Uryū, J.D.E. Creighton, and J.L. Friedman, *Phys. Rev. D* **79**, 124033 (2009).
- [41] M. Shibata and K. Uryū, *Phys. Rev. D* **74**, 121503 (2006).
- [42] M.D. Duez, F. Foucart, L.E. Kidder, C.D. Ott, and S.A. Teukolsky, *Classical Quantum Gravity* **27**, 114106 (2010).
- [43] F. Pannarale, L. Rezzolla, F. Ohme, and J.S. Read, [arXiv:1103.3526v1](https://arxiv.org/abs/1103.3526v1).
- [44] K. Kyutoku, M. Shibata, and K. Taniguchi, *Phys. Rev. D* **82**, 044049 (2010).
- [45] B.D. Lackey, K. Kyutoku, M. Shibata, P.R. Brady, and J.L. Friedman, [arXiv:1109.3402v1](https://arxiv.org/abs/1109.3402v1).
- [46] S. Chawla, M. Anderson, M. Besselman, L. Lehner, S.L. Liebling, P.M. Motl, and D. Neilsen, [arXiv:1006.2839v2](https://arxiv.org/abs/1006.2839v2).
- [47] Z.B. Etienne, Y.T. Liu, V. Paschalidis, and S.L. Shapiro, [arXiv:1112.0568v3](https://arxiv.org/abs/1112.0568v3).
- [48] F. Foucart, M.D. Duez, L.E. Kidder, M.A. Scheel, B. Szilagyi, and S.A. Teukolsky, [arXiv:1111.1677v2](https://arxiv.org/abs/1111.1677v2).
- [49] W.E. East, F. Pretorius, and B.C. Stephens, [arXiv:1112.3094v1](https://arxiv.org/abs/1112.3094v1).
- [50] F. Löffler, L. Rezzolla, and M. Ansorg, *Phys. Rev. D* **74**, 104018 (2006).
- [51] H. Friedrich, *Commun. Math. Phys.* **100**, 525 (1985).
- [52] D. Garfinkle, *Phys. Rev. D* **65**, 044029 (2002).
- [53] F. Pretorius, *Classical Quantum Gravity* **22**, 425 (2005).
- [54] C. Gundlach, J.M. Martin-Garcia, G. Calabrese, and I. Hinder, *Classical Quantum Gravity* **22**, 3767 (2005).
- [55] F. Pretorius, *Phys. Rev. Lett.* **95**, 121101 (2005).
- [56] M.W. Choptuik and F. Pretorius, *Phys. Rev. Lett.* **104**, 111101 (2010).
- [57] L. Lindblom and B. Szilagyi, *Phys. Rev. D* **80**, 084019 (2009).
- [58] A. Harten, P.D. Lax, and B.J. van Leer, *SIAM Rev.* **25**, 35 (1983).
- [59] A. Tchekhovskoy, J.C. McKinney, and R. Narayan, *Mon. Not. R. Astron. Soc.* **379**, 469 (2007).
- [60] M. J. Berger and J. Oliger, *J. Comput. Phys.* **53**, 484 (1984).
- [61] M.J. Berger and P. Colella, *J. Comput. Phys.* **82**, 64 (1989).
- [62] G.D. Quinlan and S.L. Shapiro, *Astrophys. J.* **321**, 199 (1987).
- [63] James M. Lattimer and M. Prakash, [arXiv:1012.3208v1](https://arxiv.org/abs/1012.3208v1).
- [64] F. Ozel, D. Psaltis, R. Narayan, and J.E. McClintock, [arXiv:1006.2834v2](https://arxiv.org/abs/1006.2834v2).
- [65] M. Turner, *Astrophys. J.* **216**, 610 (1977).
- [66] P. Demorest, T. Pennucci, S. Ransom, M. Roberts, and J. Hessels, *Nature (London)* **467**, 1081 (2010).
- [67] K. Glampedakis and D. Kennefick, *Phys. Rev. D* **66**, 044002 (2002).
- [68] Frans Pretorius and Deepak Khurana, *Classical Quantum Gravity* **24**, S83 (2007).
- [69] M. J. Rees, *Nature (London)* **333**, 523 (1988).
- [70] W. Kastaun, B. Willburger, and K.D. Kokkotas, *Phys. Rev. D* **82**, 104036 (2010).
- [71] K.D. Kokkotas, T.A. Apostolatos, and N. Andersson, *Mon. Not. R. Astron. Soc.* **320**, 307 (2001).
- [72] Christopher P.L. Berry and Jonathan R. Gair, *Phys. Rev. D* **82**, 107501 (2010).
- [73] K. Glampedakis and D. Kennefick, *Phys. Rev. D* **66**, 044002 (2002).
- [74] Neil J. Cornish and Janna J. Levin, *Classical Quantum Gravity* **20**, 1649 (2003).